***ChemSearch Journal 15(1): 219 – 237, June, 2024***
Publication of Chemical Society of Nigeria, Kano Chapter

Received: 12/06/2024 Accepted: 21/06/2024
http://www.ajol.info/index.php/csj

# Photocatalytic Studies of Methylene Blue Dye Degradation on Synthesized Ni-doped Strontium Zirconate Perovskite Nanoparticles

**J. N. Tsaviv[a*], I. S. Eneji[b], R. Shato'Ato[a], I. Ahemen[b], P. R. Jubu[b] and Y. Yusof [c]**

[a]Department of Chemistry, Joseph Sarwuan Tarka University, P.M.B. 2373 Makurdi, Benue State, Nigeria
[b]Department of Physics, Joseph Sarwuan Tarka University, P.M.B. 2373 Makurdi, Benue State, Nigeria
[c]Nano-optoelectronic Research Laboratory, School of Physics, Universiti Sains Malaysia, 11800, Pinang, Malaysia

***Correspondence Email:** doochivir@gmail.com

## ABSTRACT

Perovskite oxides have been recognized as highly potent catalysts for photocatalytic water decontamination due to their potential to capture solar energy and drive catalytic reactions. In this report, Ni doped strontium zirconate perovskite photocatalyst nanoparticles was synthesized using simple method with low production cost was applied in visible light irradiation for the photocatalytic degradation of a model organic pollutant in aqueous medium. The photocatalyst was synthesized successfully using sol-gel Pechini method and annealed at 800 ℃ for 2 h. The sample was characterized using XRD, FESEM, EDX FTIR and UV-visible spectrophotometric techniques. The crystallite size ranged between 23.74 and 33.18 nm according to Scherrer equation and Williamson-Hall methods with a dislocation density, lattice strain, and microstrain of 1.77, 1.4 and 3.4 (x $10^{-3}$) respectively. The sample exhibited smooth surface with no agglomeration. The composition of the perovskite indicated the presence of Sr, Zr, Ni and oxygen in their atomic weight. Metal-oxygen vibration was located at 648.55 $cm^{-1}$ with traces of adsorbed atmospheric $CO_2$ and $H_2O$ on the catalyst surface. The catalyst exhibited optical band gap energy of 5.15 eV. The photocatalytic activity was evaluated by the degradation of Methylene blue (MB) under simulated light at 420 nm. Photodegradation was highest in light irradiated reaction compared to dark conditions. The effects of the amount of catalyst, initial concentration of MB dye irradiation time and solution pH on the degradation and removal efficiency of the pollutant was investigated. Adsorption capacity was found to increase with increase in initial adsorbate concentration and irradiation time in acidic pH. In order to investigate the efficiency of MB dye adsorption on strontium nickel zirconate (SNZ) photocatalyst, pseudo-first order (PFO), pseudo-second order (PSO), Elovich and Intra-particle diffusion (IPD) kinetic models were evaluated. The adsorption kinetic was found to follow pseudo-second order model. The graphical correlation of equilibrium data were analyzed by Langmuir, Freundlich, Dubinin-Radushkevich (D-R), Temkin, Flory-Huggins and Redlich-Peterson models by using linear regression technique. The data were best represented by the Langmuir isotherm yielding maximum monolayer adsorption at 30 ℃ with a favorable condition ($R_L$ < 1). The adsorption process was found to be exothermic and spontaneous. Therefore, $Sr(Ni_{0.10}Zr_{0.90})O_3$ nanoparticles can be used as photocatalyst for remediation of wastewater containing organic pollutants.

**Keywords**: $Sr(Ni_{0.10}Zr_{0.90})O_3$, Perovskite, Photodegradation, Pechini, Williamson-Hall

## INTRODUCTION

In recent times, environmental contamination and energy shortages have been considered as two primary challenges for humans. Achieving clean and safe water is a basic asset for a flourishing society as well as a thriving economy (Jain *et al*., 2021). In view of this, access to clean water has been a militating issue for all forms of life particularly for developing and populated communities (Askari *et al*., 2024). Achieving environmental sustainability is an ultimate global challenge, and therefore requires more scientific focus towards this direction. The release of effluents from industries and human activities are turning surface water worse day by day because of the direct disposal of organic and human waste. Nakada *et al*. (2016) reported the quality of surface waters in lowland rivers of densely populated developed countries to be largely dependent on the efficiency of wastewater treatment and disposal models. Several modeling approaches have been developed to assist in water quality management. Wei *et al*. (2021) reported solar energy as one of the alternative sources of energy which is particularly clean, easily available, and accessible for wastewater treatment. The solar spectrum is the range of electromagnetic radiation emitted by the sun, extending from the ultraviolet to the infrared region. It is composed of photons with various wavelengths, which define the spectrum's shape and intensity. The use of solar energy to catalyze the photo-driven processes has attracted

tremendous attention from the scientific community because of its great potential in addressing energy and environmental issues. In this regard, several attempts have been made in the scientific world to design and develop different nanomaterials for solar energy harvesting with good photon absorption for wastewater remediation and environmental cleaning.

In solar energy harvesting, photothermal, photovoltaic, and photocatalysis are the three different approaches, which are involved in power generation and environmental remediation (Zhang *et al*., 2017; Habisreutinger *et al*., 2013). Among these, photocatalytic degradation is an emerging field which has a huge potential for the transformation of organic pollutant in wastewater (Wu *et al*., 2017). Photocatalysts have been widely reviewed for various energy and environmental applications including $H_2$ production, degradation of organic pollutants, bacteria disinfection, and $CO_2$ reduction (Bae *et al*., 2014). The photcatalytic remediation of contaminated water has been extensively investigated to demonstrate its viability as a useful cleaning process. Semiconductor materials such as perovskites have been reported as promising photocatalyst nanomaterials for wastewater treatment (Zeng, *et al*., 2018; Kong *et al*., 2019).

The photocatalytic degradation of pollutants in wastewater is one of the attractive strategies for combating water pollution problem (Luo *et al*., 2019). This process is more reliable in comparison to the conventional adsorbents like active charcoal, metal organic frameworks, silica gel, and so on, because the recycling process of these adsorbents is expensive (Kumar *et al*., 2017). Also, the chemicals and solvents used in the recycling process are generally non-green, costly, and generate secondary pollution. However, the photocatalytic degradation technique is different because it utilizes the advanced oxidation process for the degradation, in which the highly reactive species generated during photocatalysis attacks the organic pollutant molecules and oxidize them in a shorter time (Singh *et al*., 2020). Generally, the photocatalytic degradation of organic pollutants ends up in complete mineralization or low-molecular-weight products. Also, the recyclability of the catalyst is easy because of their heterogeneous nature and self-cleaning surfaces, as all reactions happen at the surface of the catalyst followed by the desorption of products. Therefore, this process can be considered as an eco-friendly and green alternative to resolve the water pollution crises. Jiang *et al*. (2019) reviewed sunlight-driven photocatalysis on semiconductor nanomaterials as a sustainable and promising technology to directly eliminate various pollutants from environmental wastewater. Fabrication of the nanomaterials, which are capable of driving desired reactions by harvesting visible solar radiation including remediation of pollutants from the environment, is one of the thrust areas of research (Subramanian *et al*., 2020). MB has been reported in the textile industry, medicine, as an indicator, oxygen and ozone sensor (Trocha *et al*., 2021) and has become an important organic contaminant in surface water, which poses a huge threat to human health and ecosystem, hence, there is keen attention towards its photocatalytic degradation from wastewater (Jiang *et al*., 2018; Wang *et al*., 2017).

$SrZrO_3$ has been utilized extensively in the field of photosplitting of water (Rojas-Cervantes and Castillejos, 2019; Hu, *et al*., 2020). However, there is no work on the photocatalytic activity of $Sr(Ni_{0.1}Zr_{0.90})O_3$ on the degradation of organic pollutants in aqueous medium. In this work, MB has been chosen as a model organic pollutant to investigate it's photodegradation by $Sr(Ni_{0.1}Zr_{0.90})O_3$ photocatalyst in presence of $H_2O_2$ under visible light irradiation.

## MATERIALS AND METHODS

### Reagents

All the chemicals used were of analytical grade. $Sr(NO)_2$ 99% (BDH Chemicals Ltd, Poole, England), Zirconium (iv) propoxide ($Zr(OC_3H_7)_4$), 98 % purity; Methylene blue, $CH_3COOH$ 99%, ethylene diamine tertra acetic acid (EDTA) 99.5 %, ethane-1, 2- diol ($HOCH_2CH_2OH$), 99 %, and citric acid ($H_3C_6H_5O_7$) 99 % and $Ni(NO_3)_2$ were purchased from Sigma Aldrich Co. 3050 Spruce Street, St. Louis MO, 63103, USA. $C_2H_5OH$ (99.5 %; S.G = 0.7951 g/mL), $H_2SO_4$ (98 %, S.G =1.84 g/mL), $H_2O_2$ (30%), and acetone (99 %; S.G = 0.789- 0.792 g/mL were purchased from Bristol Scientific, Lagos.

### Synthesis of $Sr(Ni_{0.10}Zr_{0.90})O_3$ nanoparticles

The Sol-gel Pechini method was used to prepare $Sr(Ni_{0.10}Zr_{0.90})O_3$ (Andrades *et al*., 2018; Lucena *et al*., 2017). Firstly, 5 mL zirconium iso-propoxide (Zr-n-p) was reacted with 0.5M (40 mL) citric acid and stirred for 2 h at 37 ℃ followed by the addition of 5 mL (0.5 M) $Ni(NO_3)_2$ solution with continues stirring. Thereafter, the temperature was increased to 80 °C to aid dissolution. Secondly, in another beaker, 20 mL (0.1M) of $Sr(NO_3)_2$ was dissolved in 22 mL of 0.2 M EDTA solution. The Sr-EDTA solution was stirred for 2 h at 60 °C then it was added to the $Zr^{+4}$ + $Ni^{2+}$ solution with continuous stirring and heated to 100 ℃ for 2 h. Next, was the addition of 23 mL ethane-1, 2-diol to EDTA - citric acid complex, then, the temperature of the solution was raised to 120 °C The gel was dried at 400 °C for 4 h and further annealed at 800 °C for 2 h. The synthesized flake was milled into a fine powder for characterization.

### Characterization

#### *Structural Analysis*

The crystal phase was investigated by high-resolution X-ray diffractometer (HR-XRD, PAnalytical X'Pert Pro) operating at 40 kV and 40

mA with Cu K$\alpha$ radiation (1.54060 Å) from 10 to 90° (2$\theta$ angle) using a step size of 0.05° and a counting time of 0.5 s per step at 25 ℃ at Nano-optoelectronic Research Laboratory, School of Physics, Universiti Sains Malaysia, 11800, Pinang, Malaysia. The crystallite size was determined as reported in Equations 1 and 2 (Katyayan and Agrawal, 2017; Huang *et al*., 2009):

$$D = \frac{k\lambda}{\beta \cos\theta} \quad (1)$$

where D is the Scherer's size or average crystallite size, $\lambda$ = 0.1541 nm is wavelength of the x-ray source for Cu $k_\alpha$, $\beta$ = FWHM (in radians), $\theta$ is the Bragg's angle, k is a shape factor numerically equal to 0.9.

$$\beta_{hkl} \cos\theta = \left(\frac{k\lambda}{D_{W-H}}\right) + 4\varepsilon_{W-H} \sin\theta \quad (2)$$

$$D_{W-H} = \frac{k\lambda}{Y_{intercept}} \quad (3)$$

where $D_{W-H}$ is the W-H size or crystallite size, and $\varepsilon_{W-H}$ is the Williamson-Hall microstrain determined from W-H plot. The dislocation density, lattice strain and microstrain were determined according to Equations (4- 6):

$$\delta = \frac{1}{D^2} \quad (4)$$

$$\varepsilon = \frac{\beta \cos\theta}{4} \quad (5)$$

$$s = \frac{d}{D\sqrt{12}} \quad (6)$$

**Morphological Characterization**

The surface morphology was determined using field-emission scanning electron microscope (FE-SEM, FEI Nova NanoSEM 450) at a voltage of 20 kV while elemental composition was obtained using energy dispersive X-ray spectrometer (EDX) attached to the FE-SEM at Nano-optoelectronic Research Laboratory, School of Physics, Universiti Sains Malaysia, 11800, Pinang, Malaysia (Jubu *et al*., 2020).

**Functional Characterization**

The FT-IR spectrum was probed between 4000-400 $cm^{-1}$ using Agilent Technologies (Carry 630 FTIR) with the processing soft Omic 7.3 to access bond formation at Ahmadu Bello University, Zaria, Multi User Science Research Laboratory.

**Optical Characterization**

UV-visible spectroscopy was performed using Jenway 7415 in the wavelength range of 200-800 nm to obtain the absorption spectrum of the synthesized perovskite. The band gap was determined according to Tauc's plot by extrapolating the linear segment of the curve to the $h\nu$ axis in a plot of $(\alpha h\nu)^2$ versus $h\nu$, Equation 7.

$$\alpha h\nu = C\left(h\nu - E_g\right)^m \quad (7)$$

where $E_g$ is the optical bandgap energy, $h\nu$ is the photon energy, α is the absorption coefficient, *C* is a constant, and *m* is a factor that depends on the type of allowed electronic transition and is numerically equal to $\frac{1}{2}$ for a direct allowed electronic transition. Other optical parameters such as steepness parameter, electron-phonon interaction, conduction and valence band potential edges as well as refractive index was determined (Vettumperumal *et al*., 2016; Singh *et al*., 2019; Bhardwaj *et al*., 2017).

Bulk density was determined by tapping using Pioneer Ohaus Analytical weighing balance (Eneji *et al*., 2016). Optical and bulk density was determined at Instrumental Laboratory, Department of Chemistry, College of Physical Sciences, Joseph Sarwuan Tarka University, Makurdi, Nigeria.

**Photocatalytic Test**

The photocatalytic activity of the catalyst was tested for the degradation of a model pollutant (MB dye) under visible and dark irradiations in a photoreactor made of wooden box with dimensions of 50 x 30 x 60 (L x W x H) (Bae *et al*., 2024). Artificial irradiation was provided by a 500 W Halogen arc lamp. In dark photocatalytic test, 200 mg of $SrZrO_3$ was added to 50 mL of 5 mg/L MB. The suspension was cycled under darkness for 1 h at 250 rpm, and 2 mL $H_2O_2$ was added. Then 5 mL of the suspension was withdrawn for every 30 min and centrifuged at 16000 rpm for 10 min to determine residual MB (mg/L). In a similar way, 200 mg of Ni-$SrZrO_3$ was added to 50 mL of 5 mg/L MB in a 250 mL photoreactor mounted on a cyclic vibrator. The suspension was cycled under dark for 1 h, then 2 mL of 2 mM $H_2O_2$ was added and irradiated with 500 W Halogen arc lamp (Beijing Au Light Technology Co.) with a cutoff filter (λ > 420 nm) with constant cycling from 0 to150 min. During the irradiation time, 5 mL of the suspension was withdrawn for every 30 min interval and centrifuged at 16000 rpm for 10 min to monitor the rate of photodegradation. The residual concentration of MB dye in the suspension was monitored using UV-Visible spectrophotometer at 664 nm (Kumar *et al*., 2017; Yazdanbakhsh *et al*., 2011). The parameters understudy includes, catalyst dosage, MB concentration, reaction time and solution pH at constant temperature (30 ℃). Triplicate analysis was performed for each scenario. The equilibrium concentration ($C_e$) was evaluated from the slope of the calibration curve. The adsorption capacity ($q_t$) was calculated using Eq. 8.

$$q_t = \frac{(C_0 - C_e)V}{1000m} \quad (8)$$

where $q_t$ (mg/g) is the amount adsorbed at time t, V ($cm^{-1}$) is the volume of the solution, and m (g) is the mass of photocatalyst. The photo-degradation efficiency (D%) was obtained using Eq.9.

$$D\ (\%) = \frac{C_o - C_t}{C_0} \times 100 \quad (9)$$

where D (%) represents the percentage degradation efficiency, $C_o$ and $C_t$ are the initial and final concentration, respectively at a given time (mg/L). The concentration of MB dye was evaluated using a five-point calibration curve ranging from 0 to 25 mg/L.

**Adsorption Kinetics Models**

Adsorption kinetics is a fundamental aspect of analyzing the adsorption mechanism. The kinetics of adsorption of MB dye on $Sr(Ni_{0.10}Zr_{0.90})O_3$ nanoparticles was studied using the PFO, PSO and Elovic model, as well as intraparticle diffusion model. The experimental data were fitted into the models to investigate the mechanism of adsorption, photodegradation and rate limiting step (Abebe *et al*., 2018).

**First-order Kinetic Model**

The experimental data were fitted with the linear form of PFO rate equation (Eqn. 10) (Eneji *et al*., 2016) while the half-life ($t_{1/2}$) was determined according to Eqn. (11):

$$\log(q_e - q_t) = (\log q_e) - \frac{k_1}{2.303}\, t \quad (10)$$

$$t_{1/2} = \frac{\ln 2}{k_1} \quad (11)$$

where $q_e$ and $q_t$ (mg/g) are amounts of MB dye adsorbed at equilibrium at any time t, (min), respectively and $k_1$ ($min^{-1}$) is the adsorption rate constant.

**Pseudo Second Order**

Experimental data were also tested by PSO kinetic model which is given (Eqn 12) as:

$$\left[\frac{t}{q_t}\right] = \frac{1}{h} + \frac{1}{q_e}(t) \quad (12)$$

From the equation, the linear plot of $\frac{t}{q_t}$ versus t gave $1/q_e$ as the slope and $1/k_2q_e^2$ as the intercept. The second-order rate constant was used to evaluate the initial sorption rate and half-life as shown in Eqns. 13 & 14:

$$h = k_2(q_e{}^2) \quad (13)$$

$$t_{1/2} = \frac{1}{k2[A]_0} \quad (14)$$

where $k_2$ (g/mg min) is the rate constant of second-order adsorption.

**Elovic Kinetic Model**

To understand whether a system is chemisorptive or not, Elovich model (developed by Zeldowitsch) was applied. This model helps to predict the mass and surface diffusion, activation and deactivation energy of a system. Although the model was initially applied in gaseous systems, its applicability in wastewater processes has been redeemed meaningful. The model assumes that the rate of adsorption of solute decreases exponentially as the amount of adsorbed solute increase (Kajjumba *et al*., 2018). The linearized form (Edet and Ifelebuegu, 2020) is expressed in Eqn (15):

$$q_t = \frac{1}{\beta}\ln(\alpha\beta) + \frac{1}{\beta}\ln(t) \quad (15)$$

where α and β are constants obtained from the slope and intercept of the linear plot of $q_t$ against ln t.

**Intra Particle Diffusion (IPD) Model**

The IPD model (Patil *et al*., 2012) is expressed in Eqn. (16):

$$R = K_{id}t^a \quad (16)$$

where *t* is the time of contact (h), *R* is the percentage of MB adsorbed and *a* is the linear plot gradient and depict the mechanism(s) of adsorption.

$K_{id}$ is the intra-particle diffusion rate constant ($h^{-1}$) and could be taken as rate factor (% removed per unit time). The Linear form is depicted in Equation (17):

$$q_t = K_{id}t0.5 + \beta \quad (17)$$

values of $K_{id}$ can be obtain from slope of the plot of $q_t$ against $t^{0.5}$.

where $K_{id}$ and β are the intraparticle diffusion rate constant and mechanism of sorption respectively.

**Adsorption Isotherms**

In this study, Langmuir, Freundlich, D-R, Temkin, Flory-Huggins and Redlich-Peterson (R-P) models were used to evaluate the equilibrium data for adsorption and degradation of MB dye on the photocatalyst in aqueous solution (Hameed *et al*., 2008).

**Langmuir Model**

The linear form of the Langmuir isotherm assuming a monolayer adsorption on a homogeneous adsorbent surface, is expressed as:

$$\frac{C_e}{q_e} = \frac{1}{bq_m} + \frac{C_e}{q_m} \quad (18)$$

where $q_m$ (mg/g) is the surface concentration at monolayer coverage which illustrates the maximum value of $q_e$ and it can be attained as $C_e$ is maximum. The b parameter is a coefficient related

to the energy of adsorption and increases with increasing strength of the adsorption bond.

**Freundlich Model**

Freundlich model is an empirical equation based on sorption on a heterogeneous surfaces or surfaces supporting sites of varied affinities. The equation is expressed linearly as:

$$\log q_e = \log K_F + \frac{1}{n} \log C_e \quad (19)$$

where $K_F$ and n are constants of the Freundlich related to sorption capacity and sorption intensity of the catalyst for a unit equilibrium concentration.

**Dubinin Radushkevich (D-R)**

The Dubinin–Radushkevich isotherm is more general than the Langmuir isotherm because it does not assume a homogeneous surface or constant adsorption potential. It is applied to distinguish between the physical and chemical adsorptions. This model makes approximations for porosity, free energy, and adsorbent properties. It helps identify the type of adsorption that took place and the apparent energy of adsorption. It's linear and free energy is expressed in Equations 20 & 21 (Edet and Ifelebuegu, 2020).

$$\ln q_e = ln q_m - B_D [RT ln\left(1 + \frac{1}{C_e}\right)]^2 \quad (20)$$

$$E = \frac{1}{\sqrt{2B}} \quad (21)$$

where the maximum adsorption capacity is denoted by $q_m$ (mol/g) and the D-R constants $B_D$ ($mol^2/kJ^2$) i.e the free energy of sorption per mole of the adsorbate as it approaches the adsorbent surface are obtained from the slope and intercept of the linear plot of Equation 20.

**Temkin Model**

The Temkin isotherm assumes that the heat of adsorption of all the molecules in the layer would decreases linearly with increasing coverage of the adsorbate on the surface of adsorbent, incorporating a factor that accounts for the indirect interaction between adsorbate molecules due to the adsorbent's surface heterogeneity (Obaid, 2020). The model is expressed linearly:

$$q_e = \frac{R_T}{b} ln K_t + \frac{R_T}{b} ln C_e \quad (22)$$

where T is the absolute temperature, R is the ideal gas constant, and $K_t$ ($dm^3/g$) is the equilibrium binding energy, or the optimum binding energy. A constant called $b_T$ (J/mol) is connected to the heat of adsorption.

**Flory-Huggin**

This isotherm describes the degree of surface coverage characteristics of the adsorbate on the adsorbent. The linear form is expressed in Equation (23) (Nechifor *et al*., 2015):

$$\ln \frac{\theta}{C_o} = \ln K_{FH} + n \ln (1- \theta) \quad (23)$$

where θ is the degree of surface coverage, n is number of adsorbates occupying adsorption site, and $K_{FH}$ is Flory-Huggins equilibrium constant (L $mol^{-1}$). This isotherm model can express the feasibility and spontaneity of an adsorption process. The equilibrium constant $K_{FH}$ was used to calculate spontaneity Gibbs free energy as shown in Equation (24):

$$\Delta G^0 = RT \ln (K_{FH}) \quad (24)$$

where $\Delta G^0$ is standard free energy change, R is 8.314 J $mol^{-1}$ $K^{-1}$, and T is absolute temperature.

**Redlich-Peterson Model**

The Redlich-Peterson equation is used as a compromise between Langmuir and Freundlich systems. The model has three parameters and incorporates the advantageous significance of both Langmuir and Freundlich models. According to Musah *et al*. (2018), the model provides a more accurate prediction of adsorption system that functions across a variety of concentrations. Equation (25) illustrates the linear expression:

$$\ln \frac{C_c}{q_e} = g ln C_e - ln K_R \quad (25)$$

where $g$ represents exponent between 0 and 1. A plot of $\ln \frac{C_e}{q_e}$ vs $\ln C_e$ is used to obtain $g$ and $\ln K_R$.

## RESULTS AND DISCUSSION

**Phase analysis**

Fig. 1 depicts the XRD pattern of the $Sr(Ni_{0.10}Zr_{0.90})O_3$ nanoparticles treated at 800 ℃ for 2 h. The peaks were sharp, indicating high crystallinity. Peak profile analysis was carried out using Debye Scherrer and Williamson-Hall (W-H) method (Fig. 1b). The diffraction peaks at 2θ angles appeared 27.82°, 29.18°, 29.93°, 31.04°, 32.45°, 33.71°, 36.68°, 37.99°, 40.25°, 41.46°, 44.18° and 46.23° can be assign to scattering from the (121), (202), (202), (202), (212), (103), (131), (222), (123), (123), (400) and (141) planes of the perovskite crystal lattice, respectively. The peaks of XRD confirms clearly that the phases belong to $Sr(Ni_{0.10}Zr_{0.90})O_3$ and match well with the phase reported in the powder diffraction data. It is found that $Sr(Ni_{0.10}Zr_{0.90})O_3$ crystallized in the orthorhombic structure with $\alpha$ = 8.2532, b= 8.2662 and c = 8.2709 Å and a space group *Bmmb* according to Mantwa *et al*. (2018). Alfonso-Herrera *et al*. (2018) reported lower average crystallite size for $SrZrO_3$ annealed in air at 800 ℃ for 8 h. The result of the structural parameters of $Sr(Ni_{0.10}Zr_{0.90})O_3$ nanoparticles is shown in Table 1.

Table 1: Structural and Optical Parameters of $Sr(Ni_{0.10}Zr_{0.90})O_3$ Nanoparticles

| Structural Parameter | Structural Magnitude | Optical Parameter | Optical Magnitude (eV) |
|---|---|---|---|
| 2θ | 32.399 | $E_g$ | 5.15 |
| FWHM | 0.3447 | n | 0.6910 |
| d-spacing (nm) | 0.2760 | $\sigma$ $(10^{-21})$ | 1.2268 |
| Crystallite Size (S) (nm) | 23.74 | $E_{(e-p)}$ $(10^{-20})$ | 5.4342 |
| Crystallite size (W-H) (nm) | 33.18 | $E_{cb}$ | -5.4681 |
| Microstrain (ε) $(10^{-3})$ | 3.4 | $E_{vb}$ | -0.3381 |
| Lattice strain (ή) $(10^{-3})$ | 1.4 | | |
| Dislocation density $(/m^{-2})$ $(10^{-3})$ | 1.77 | | |
| Bulk density (g/mL) | 0.2130 | | |
| Cell vol. $A^3$ $(x10^6\ pm^3)$ | 68.57 | | |

where: S = Scherer's, W-H = Williamson-Hall , $E_g$= Energy band gap, n= refractive index, $\delta$ = steepness parameter, $E_{e-p}$ = electron phonon interaction energy, $E_{cb}$= conduction band energy, $E_{vb}$ = valence band energy

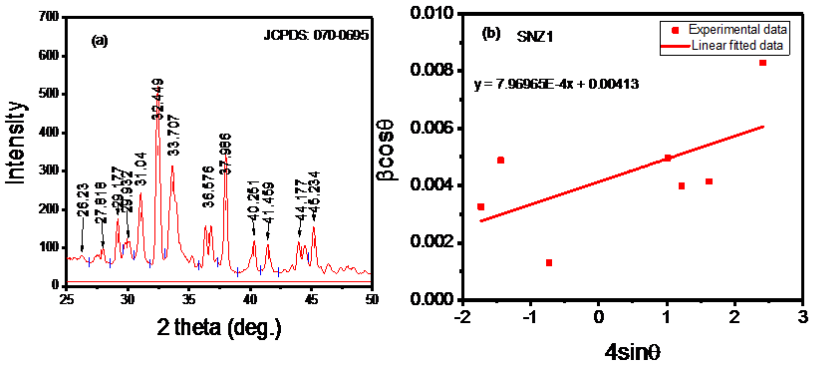


**Fig.1. (a) XRD pattern, (b) Williamson-Hall plot of the $Sr(Ni_{0.10}Zr_{0.90})O_3$ photocatalyst**

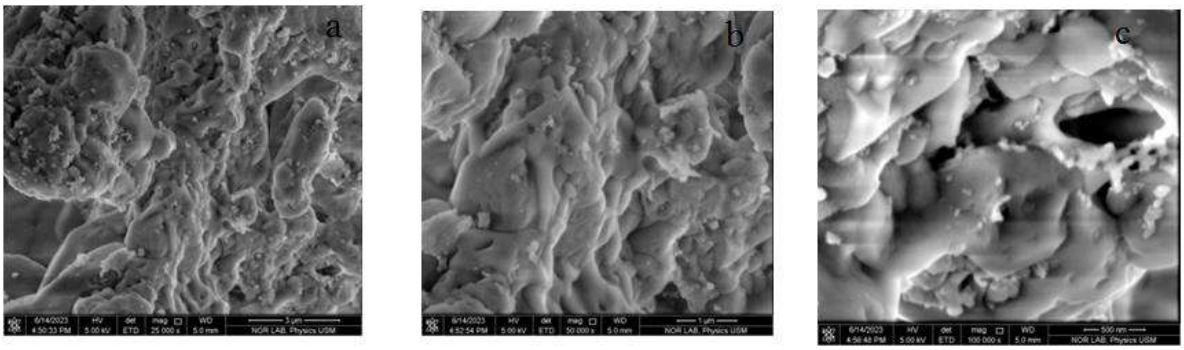


**Fig. 2. FESEM images of $Sr(Ni_xZr_{1-x})O_3$ at (a) 25,000, (b) 50,000 and (c ) 100,000 Magnifications.**

**Surface Morphology**

The surface morphology of the sample was recorded at 25,000, 50,000 and 100,000 magnifications (Fig. 2). The surface is smooth with irregular shape and is in agreement with the result of the bulk density (Table 1). Lower particle size enhances more reactivity and prevents recombination reactions (Tarrida *et al*., 2009; Jubu *et al*., 2020).

**Fourier Transform Infrared Spectroscopy**

Fig. 3(a & b) displays the full and zoom FTIR spectrum $Sr(Ni_{0.10}Zr_{0.90})O_3$ nanoparticles recorded between 4000-400$cm^{-1}$. The vibration bands were located at 648.58, 1204.83, 1561.60, 2963.41, 3211.58, 3253.88 and 3785.33 $cm^{-1}$. The band located at 648.58 (Fig. 3b) could be related to the molecular vibration of metal – oxygen band associated to strontium-oxygen (Sr-O) bonds. The absorption peak with high intensity centered at 1204.83 $cm^{-1}$ could be due to the existence of vibration mode of Zr-O. This absorption peak could be connected to the stretching vibration involving the internal motion of changes in the bond length of Zr-O band; and this relationship verifies the occurrence of $ZrO_6$ octahedral deformation in the compound. Utami *et al*. (2019) reported absorption bands of 400-600 $cm^{-1}$ as asymmetric stretching and bending vibrations of the metal-oxygen bond in perovskite structures. The band at approximately 1561.60 $cm^{-1}$ could be due to surface adsorbed $CO_2$. The band range from 2963.41 – 3785.33 $cm^{-1}$ could be due to surface adsorbed moisture. Triyono *et al*. (2020) reported spectral bands above 2000 $cm^{-1}$(O-H bond) to stretching vibrations of absorbing ambient

moisture. Katyayan and Agrawal (2017) reported FTIR band range of 3633-3905 $cm^{-1}$ to be minute traces of moisture (O-H). Ouni *et al.* (2012) reported shift in vibration frequencies, band positions and absorption peaks to be influenced by material composition, synthesis method and protocol, lattice size, microstrain and shape of the material.

**Elemental Composition**

The chemical composition of the investigated catalyst is shown in Fig. 3c. The spectrograph showed the presence of Sr, Zr, Ni and O elements in the synthesized compound.

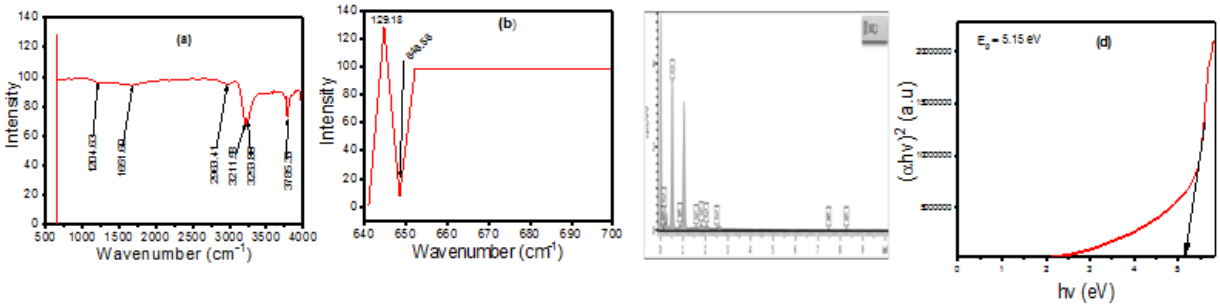


**Fig. 3 (a) Full and (b) Zoom FTIR spectrum of $SrZrO_3$ Nanoparticle (c) EDX (d) Tauc's Plot**

**Optical Properties**

Fig.3d depicts the Tauc plot for the optical band gap energy of $Sr(Ni_{0.1}Zr_{0.90})O_3$ photocatalyst. The band gap according to Tauc formula was 5.15 eV and agrees with the report of Cabello *et al.* (2014). Aside other physical and chemical properties of catalyst, changes in the optical band gap energy could occur due to doping, synthesis technology, strain, particle morphology, annealing temperature, concentration of precursors, solution pH and reactions conditions (Perumal, *et al.*, 2012). Other optical properties of the catalyst are illustrated (Table 1).

In order to access photodegradation effect, total organic carbon (TOC) was measured using Winkle-Black method. The TOC ranged between 0.1551 - 0.0600 from 0 -150 min irradiation time.

**Calibration Curve**

A five-point linear fit for MB was obtained to study the photodegradation at 664 nm. The fit was obtained using absorbance of 0-25 mg/L MB (Fig. 4a). A linear regression equation was used to estimate the equilibrium concentration of degraded MB pollutant under irradiation.

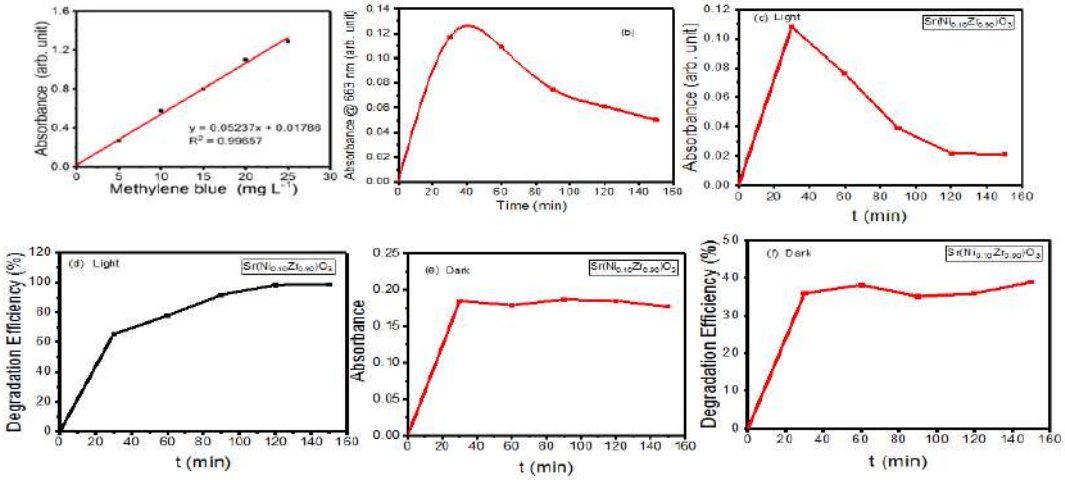


**Fig. 4: (a) Linear Fit of MB (b) Absorbance light (c) Degradation in light (d) Absorbance in dark (e) Degradation Efficiencies in dark irradiations**

**Degradation Studies**

***Absorbance and degradation studies in the dark and light illumination***

Fig. 4(b & d) illustrates the absorbance in the dark and light illumination reactions for MB dye degradation using $SrNi_{0.10}Zr_{0.90})O_3$ assisted $H_2O_2$. The initial absorbance (0.189) of MB in the dark (Fig. 4d) did not change as compared to the light illuminated reaction (Fig. 4b). In light irradiation, absorbance decreases from 0.189 to 0.080 between the time intervals of 0-150 min indicating degradation (Fig. 4c & e). The degradation efficiency in the dark and in the presence of light irradiation was 35.23 % and 80.44 %, respectively. This observation implied photocatalytic degradation increase with increased in radiation time in the presence of $H_2O_2$ (Saha *et al.*, 2018). This scenario is similar to the report of

Alammar *et al*. (2015) using $SrTiO_3$, $CaTiO_3$ and $BaTiO_3$ perovskites photocatalysts. Bellam *et al*. (2015) reported 60% degradation efficiency of 3.2 mg/L MB within 150 min using $N_2$ doped $NiTiO_3$ catalyst in visible light.

**Adsorption Kinetics**

The efficiency was investigated using a batch equilibrium technique with different amounts of catalyst in 250 mL conical flask containing 50 mL of MB. The kinetic studies were studied for different pH values, irradiation time, catalyst dosage and MB dye concentration (Itodo *et al*., 2018).

**Effect of Catalyst Dosage**

Fig. 5a showed the effect of catalyst dosage. The degradation efficiency was highest at 200 compared to 250 mg. At higher dosage (250 mg), the degradation was found to decrease. This might be due to the turbidity of the solution, which increased with the amount of catalyst loading and blocked the photons reaching the medium. This phenomenon may result to a smaller number of active photoactive species present and may consequently reduce degradation. Several studies report the photocatalytic rate to first rise along with catalyst loading and then deflate at high dosage due to unavailable active surface sites for exposure and light scattering effects (Rani *et al*., 2020).

**Effect of Irradiation Time**

The effect of contact time on degradation efficiency was examined using 50 mL of 5 mg/L MB and 200 mg catalyst from 0-150 min. Fig. 5b examines the increase in degradation due to increase in contact time until an equilibrium time is reached that led to a decrease in residual MB concentration. The highest removal efficiency was observed at above 120 min. There is no previous work on the use of $Sr(Ni_{0.10}Zr_{0.90})O_3$ coupled $H_2O_2$ for which we can compare the present report. Nevertheless, the effect of contact time on degradation of MB in various catalysts could be found in the literatures. Soltanabadi *et al*. (2018) reported the removal of rhodamine B (30 mg/L) within 90 min using visible light irradiation with assisted $H_2O_2$ for $LaFeO_3$ supported CuO. The performance of $H_2O_2$ for $LaFeO_3$was higher compared to the pure $LaFeO_3$, thus, supporting the goodness performance of synthesize catalyst. Chang and Hu (2020) reported over 70% degradation efficiency for MB, methyl orange, Rhodamine, bisphenol A and phenol using $SrTiO_3$ supported 20 wt% $Ga_2O_3$ within 3 h irradiation.

**Effect of Initial MB Concentration**

The initial dye concentration is another important variable that affect adsorption process during photocatalysis. This effect was investigated by varying the initial MB concentration (0 - 25 mg/L), using a catalyst dose of 200 mg. Results showed decreased degradation efficiency of MB with increasing initial MB concentration (Fig. 5c). This scenario could be attributed to oversaturation of the available catalyst active sites (Anas *et al*., 2023). Higher adsorption of pollutant with a high initial concentration of pollutant facilitates more pollutant molecules to get excited on light irradiation, which enhances the photodegradation efficiency. However, at higher concentration reduction in photodegradation is observed due to reduction in the number of photons reaching the catalyst surface and consequent reduction in the number of $OH^*$ radicals and positive hole generation (Boruah *et al*., 2016).

**Effect of Solution pH**

One of the most important factors affecting the capacity of adsorbent in wastewater remediation is solution pH. The efficiency of adsorption of organic pollutant is dependent on the solution pH, since variation in pH leads to the variation in the degree of ionisation of the adsorptive molecule and the surface properties of adsorbent The effect of initial solution pH on degradation and removal efficiency was evaluated at pH 3-10, while the initial MB concentration and catalyst dosage were fixed at 5 mg/L and 200 mg, respectively (Fig 5d). The degradation efficiency was found to be 80.44% in acidic pH 3 and decreased with increasing pH value. This phenomenon could be due to surface electrostatic charge, oxidative potential and sorption capacity between the dye molecule and the catalyst surface (Nguyen *et al*., 2016). Yazdanbakhsk *et al*. (2011) reported pH 2 as the optimum pH value for the removal of Reactive blue dye from aqueous solution containing Ca doped lanthanum nickel trioxide catalyst.

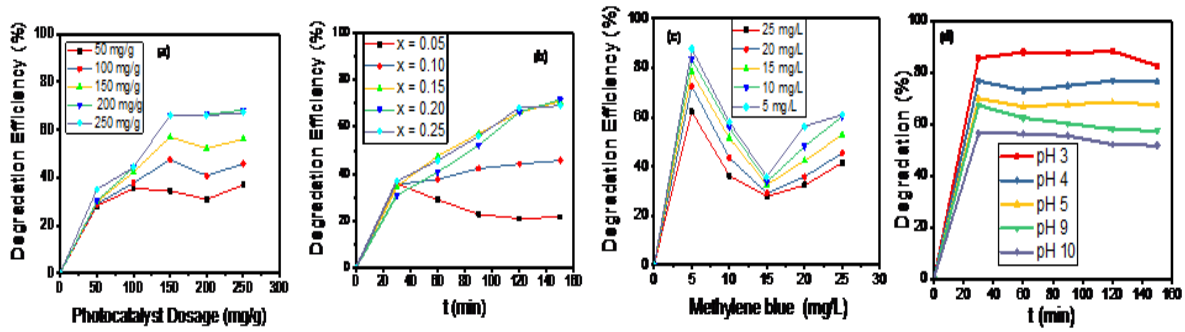


**Fig.5 (a-d): Degradation Efficiencies due to Effects of (a) Catalyst Dosages (b) Time dependent reaction (c) MB Initial concentration and (d) solution pH at different time**

**Kinetic Models**

***Pseudo-first-order***

The plot of log(*qe*−*–qt*) versus time for various catalyst dosages and MB concentrations is shown in Fig. 6(a & b) to evaluate the PFO kinetics. The constants of PFO model such as $k_1$ and $q_e$ were determined from the slope and intercept of the fitted lines, respectively. The correlation coefficient ($R^2$) for the plot decreased from 0.9878 - 0.8750 and 0.9824 - 0.9266 for the effects of catalyst dosage and MB concentrations. The calculated *qe* values from first-order kinetic were lower than the experimental $q_e$ value determined using the relation: $\boldsymbol{q_e = \frac{(C_0 - C_e)V}{1000m}}$. This demonstrates that the pseudo-first-order model was inadequate to estimate the adsorption kinetics of MB on $Sr(Ni_{0.10}Zr0.90)O_3$ nanoparticles. This scenario agrees with the review of Rashad *et al.* (2022) on adsorption study of Congo red dye from synthetic wastewater at different concentrations using ZnS Nanoparticles. The value of $k_1$ and correlation coefficient for the effects of catalyst dosage and initial MB concentration is shown in Table 2. The experimental $q_e$ values did not agree with the calculated values obtained from the linear plots. Furthermore, validation by normalized standard deviation (Table 2) showed that the adsorption of MB dye on $Sr(Ni_{0.10}Zr_{0.90})O_3$ catalyst is not a first-order reaction kinetics.

**Table 2: Adsorption kinetic parameters for the effect of catalyst dosage and initial MB for PFO at 30.05℃**

| PFO model | | Parameters | | | | | |
|---|---|---|---|---|---|---|---|
| | | $k_1$ | $q_{e\ cal}$ | $q_{e(exp)}$ | $R^2$ | $t_{1/2}$ | $\Delta q_e$ (%) |
| Catalyst dosage (mg/L) | 50 | 0.00161 | 1.6396 | 1.7512 | 0.9878 | 430.50 | 4.51 |
| | 100 | 0.00793 | 1.4304 | 1.1429 | 0.9320 | 87.40 | 17.79 |
| | 150 | 0.00834 | 1.8742 | 1.1820 | 0.9396 | 83.11 | 41.41 |
| | 200 | 0.00824 | 1.9056 | 0.8908 | 0.9009 | 84.22 | 80.55 |
| | 250 | 0.00789 | 2.8415 | 0.7283 | 0.8750 | 87.85 | 205.17 |
| Methylene blue (mg/L) | 5 | 0.00853 | 0.6099 | 1.0966 | 0.9824 | 81.25 | 31.38 |
| | 10 | 0.01132 | 0.4304 | 1.4491 | 0.9589 | 61.23 | 49.71 |
| | 15 | 0.00694 | 0.5331 | 1.3386 | 0.9553 | 99.87 | 42.55 |
| | 20 | 0.00526 | 1.9056 | 2.8130 | 0.9462 | 131.77 | 22.81 |
| | 25 | 0.00601 | 2.8415 | 4.2348 | 0.9266 | 115.32 | 23.26 |

**Pseudo-second-order**

The result of the linear plots of $t/q_t$ vs t (Fig. 6c, d & e) showed a good agreement between experimental and the calculated $q_e$ values for the effects of dosage, MB concentration and solution pH as well as sorption rate and half-life (Table 3). Besides, the correlation coefficient values for the second-order kinetic model were almost equal to unity for all the MB dye concentrations, indicating the applicability of the model to describing the adsorption of MB on the photocatalyst surface for photodegradation. The result of the comparison of the PFO and PSO adsorption rate constants and calculated experimental $q_e$ values for different initial dye concentrations (Table 4) depict that the reaction followed pseudo-second order rate.

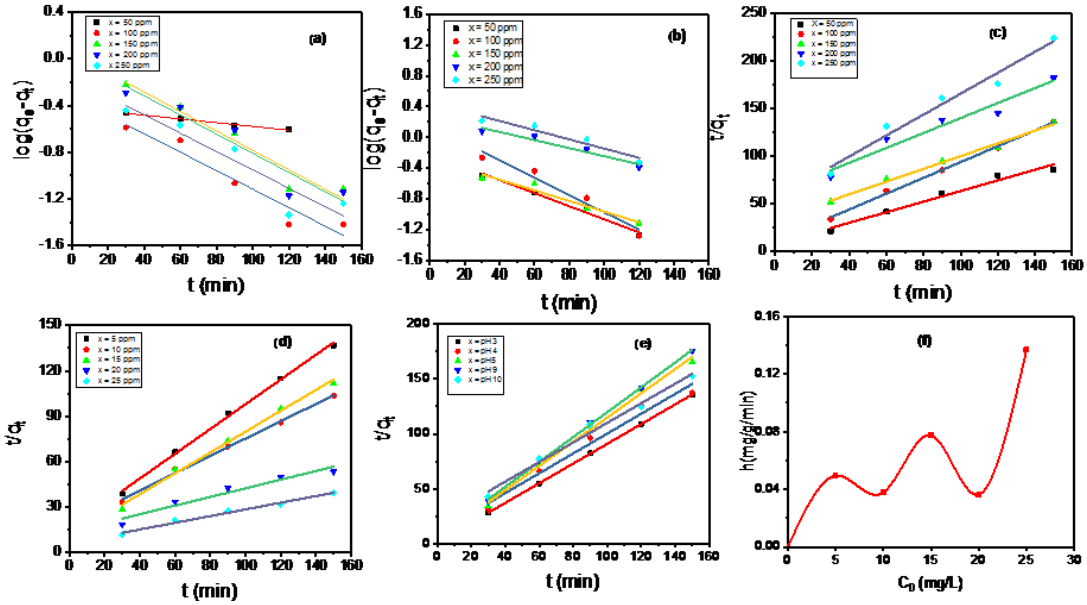


**Fig. 6: PFO (a & b) dosage and MB concentration, PSO (c, d & e) Kinetics for the Effects of dosage, concentration, Solution pH and (f) Initial sorption rate verses initial Concentration for the Degradation of MB Dye**

**Table 3: Adsorption kinetic parameters for the effects of catalyst dosage, initial MB concentration and solution pH for PSO at 30.05℃**

| | | PSO Parameters | | | | | | |
|---|---|---|---|---|---|---|---|---|
| | | $k_2$ | $q_{e\ cal.}$ | $q_{e\ exp.}$ | $R^2$ | h | $t_{1/2}$ (min) | $\Delta q_e$ (%) |
| mg | 50 | 0.0403 | 1.7962 | 1.7512 | 0.9731 | 0.1301 | 4.96 | 1.82 |
| | 100 | 0.0636 | 1.2061 | 1.1429 | 0.9997 | 0.0926 | 3.14 | 3.91 |
| | 150 | 0.0135 | 1.4973 | 1.1820 | 0.9910 | 0.0302 | 14.86 | 18.86 |
| | 200 | 0.0100 | 1.2762 | 0.8961 | 0.9490 | 0.0163 | 20.04 | 29.99 |
| | 250 | 0.0216 | 0.9113 | 0.7283 | 0.9704 | 0.0179 | 9.26 | 17.77 |
| mg/L | 5 | 0.0411 | 1.0966 | 1.2244 | 0.9978 | 0.0494 | 4.87 | 7.38 |
| | 10 | 0.0180 | 1.5491 | 1.7502 | 0.9955 | 0.0378 | 5.55 | 8.12 |
| | 15 | 0.0433 | 1.3386 | 1.4520 | 0.9927 | 0.0775 | 3.54 | 5.52 |
| | 20 | 0.0059 | 3.1712 | 3.5008 | 0.9427 | 0.0363 | 8.48 | 6.66 |
| | 25 | 0.0076 | 4.2348 | 4.5280 | 0.9857 | 0.1368 | 5.24 | 4.58 |
| pH | 3 | 0.6837 | 1.1140 | 1.1061 | 1.0000 | 0.8485 | 0.29 | 0.51 |
| | 4 | 0.0839 | 1.1050 | 1.0918 | 0.9769 | 0.1024 | 2.39 | 0.85 |
| | 5 | 0.2705 | 0.9058 | 0.9056 | 0.9952 | 0.2219 | 0.74 | 0.02 |
| | 9 | 0.1996 | 0.8823 | 0.8531 | 0.9991 | 0.1554 | 1.00 | 2.42 |
| | 10 | 0.0383 | 1.1203 | 0.9820 | 0.9858 | 0.0481 | 5.22 | 9.96 |

**Table 4: Comparison of the Pseudo-first- and second-order adsorption rate constants and calculated experimental $q_e$ values for different initial dye concentrations**

| Initial concentration ($mgL^{-1}$) | $q_{e\ exp.}$ ($mgg^{-1}$) | First order kinetic model | | | | Second order kinetic model | | | |
|---|---|---|---|---|---|---|---|---|---|
| | | $k_1$ | $q_{e\ cal.}$ | $R^2$ | $\Delta q_e$ (%) | $k_2$ | $q_{e\ cal.}$ | $R^2$ | $\Delta q_e$ (%) |
| 5 | 1.0966 | 0.00853 | 0.6099 | 0.9824 | 31.38 | 0.0411 | 1.0966 | 0.9978 | 7.38 |
| 10 | 1.4491 | 0.01132 | 0.4304 | 0.9589 | 49.71 | 0.0180 | 1.5491 | 0.9955 | 8.12 |
| 15 | 1.3386 | 0.00694 | 0.5331 | 0.9553 | 42.55 | 0.0433 | 1.3386 | 0.9927 | 5.52 |
| 20 | 2.8130 | 0.00526 | 1.9056 | 0.9462 | 22.81 | 0.0059 | 3.1712 | 0.9427 | 6.66 |
| 25 | 4.2348 | 0.00601 | 2.8415 | 0.9266 | 23.26 | 0.0076 | 4.2348 | 0.9857 | 4.58 |

**Elovic Kinetic Model**

Fig. 7 depicts the result of Elovic kinetic model for the photocatalysis of MB dye. The $R^2$ values obtained was in the range of 0.87894 - 0.99662 for MB initial concentration of 0 – 25 mg/L (Table 5). The $q_e$ calculated values do not agreed quite well with the experimental values

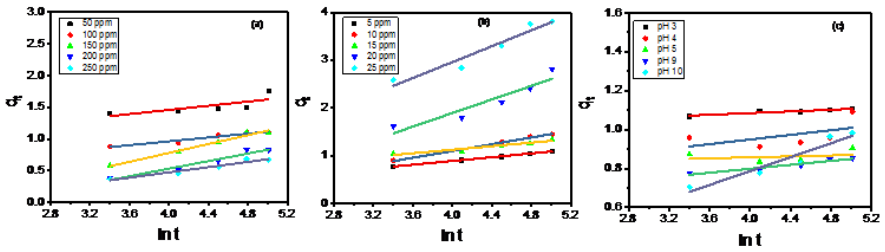


**Fig. 7: Linear Fit of Elovich Adsorption Kinetic Model for the Uptake and Degradation of MB dye on Ni doped $SrZrO_3$ Photocatalyst (a) dosages (b) MB concentrations and (c) solution pH at 30 ℃ .**

**Table 5**: **Adsorption kinetic parameters for the effect of catalyst dosage, initial MB concentration and solution pH for Elovich model at 30 ℃**

| | | Elovic Parameters | | | | |
|---|---|---|---|---|---|---|
| | | $R^2$ | 1/β | β | α | $q_{e\ exp.}$ |
| mg | 50 | 0.59687 | 0.16447 | 6.0801 | 2.2286 | 1.7512 |
| | 100 | 0.94151 | 0.15254 | 6.5557 | 1.4247 | 1.1429 |
| | 150 | 0.98172 | 0.35081 | 2.8505 | 1.8627 | 1.1820 |
| | 200 | 0.94496 | 0.29811 | 3.3545 | 1.9332 | 0.8961 |
| | 250 | 0.94282 | 0.20718 | 4.8267 | 1.4261 | 0.7283 |
| mg/L | 5 | 0.99662 | 0.19645 | 5.0904 | 1.1093 | 1.0966 |
| | 10 | 0.98554 | 0.3538 | 2.8265 | 0.7281 | 1.4491 |
| | 15 | 0.92807 | 0.18534 | 5.3955 | 1.4664 | 1.3386 |
| | 20 | 0.87894 | 0.70954 | 1.4094 | 0.3886 | 2.8130 |
| | 25 | 0.92964 | 0.8288 | 1.2066 | 0.7009 | 4.2348 |
| pH | 3 | 0.85871 | 0.02168 | 46.1255 | 2.7134 | 1.1061 |
| | 4 | 0.28838 | 0.05967 | 16.7588 | 2.0349 | 1.0918 |
| | 5 | 0.0745 | 0.01216 | 82.2368 | 2.2450 | 0.9056 |
| | 9 | 0.91005 | 0.05082 | 19.6773 | 1.8136 | 0.8531 |
| | 10 | 0.91172 | 0.17928 | 5.5779 | 1.0723 | 0.9820 |

**Intra Particle Diffusion (IPD) Model**

The result of IPD model for the adsorption and degradation of the MB dye by SNZ catalyst at 30 ℃ is reprsented in Fig. 8(a, b & c). The values of $k_{id}$ were calculated from the slope of such plots and the $R^2$ values led to the conclusion that the IPD is a rate limiting step. Higher $k_{id}$ values illustrate an enhancement in the rate of adsorption. Such high $k_{id}$ values illustrate a better mechanism, which is related to an improved bounding between the MB dye and the catalyst (Table 6) (Bello *et al*., 2010). Table 7 depicts the result of the comparison of Elovic and IPD kinetic model values for different initial MB concentrations

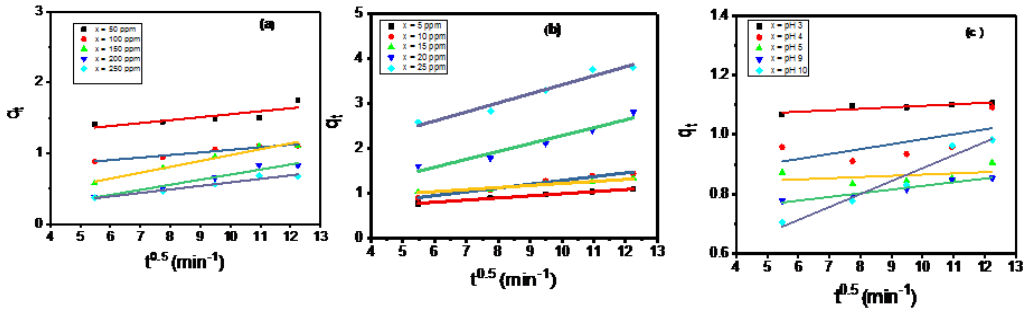


**Fig. 8**: **Linear Fit of IPD Kinetic Model for the Effect of (a) dosages, (b) MB concentration and (c) Solution pH**

**Table 6: Adsorption kinetic parameters for the effect of catalyst dosage, initial MB concentration and solution pH for IPD model at 30.05℃**

| Model | | IPD Parameters | | | |
|---|---|---|---|---|---|
| | | $R^2$ | $k_{id}$ | β | $q_{e\ exp.}$ |
| mg | 50 | 0.6818 | 0.0419 | 1.1334 | 1.7512 |
| | 100 | 0.9391 | 0.0363 | 0.6853 | 1.1429 |
| | 150 | 0.9668 | 0.0830 | 0.1449 | 1.1820 |
| | 200 | 0.9600 | 0.0716 | 0.0176 | 0.8961 |
| | 250 | 0.9534 | 0.0497 | 0.0929 | 0.7283 |
| Mg/L | 5 | 0.9949 | 0.0468 | 0.5303 | 1.0966 |
| | 10 | 0.9837 | 0.0843 | 0.7509 | 1.4491 |
| | 15 | 0.9664 | 0.0451 | 0.7766 | 1.3386 |
| | 20 | 0.9441 | 0.1753 | 0.9876 | 2.8130 |
| | 25 | 0.9588 | 0.2007 | 1.5145 | 4.2348 |
| pH | 3 | 0.8069 | 0.0050 | 1.0467 | 1.1061 |
| | 4 | 0.3914 | 0.0166 | 0.8184 | 1.0918 |
| | 5 | 0.1443 | 0.0040 | 0.8246 | 0.9056 |
| | 9 | 0.9512 | 0.0124 | 0.7031 | 0.8531 |
| | 10 | 0.9506 | 0.0437 | 0.4504 | 0.9820 |

**Table 7: Comparison of Elovic and IPD kinetic model values for different initial MB concentrations**

| **Initial concentration ($mgL^{-1}$)** | **Elovic kinetic model** | | | **IPD Kinetic model** | | |
|---|---|---|---|---|---|---|
| | **β** | **α** | $R^2$ | **$k_{id}$** | **α** | $R^2$ |
| 5 | 5.0904 | 1.1093 | 0.99662 | 0.0843 | 0.7509 | 0.9949 |
| 10 | 2.8265 | 0.7281 | 0.98554 | 0.0451 | 0.7766 | 0.9837 |
| 15 | 5.3955 | 1.4664 | 0.92807 | 0.1753 | 0.9876 | 0.9664 |
| 20 | 1.4094 | 0.3886 | 0.87894 | 0.2007 | 1.5145 | 0.9441 |
| 25 | 1.2066 | 0.7009 | 0.92964 | 0.0843 | 0.7509 | 0.9588 |

**Validity Test of Kinetic Models**

Beside the value of $R^2$, the applicability of kinetic models for the adsorption and photocatalytic degradation process was validated using normalized standard deviation, $\Delta q_e$ (%) expressed as (Bello *et al*., 2009):

$$\Delta q_e\,(\%) = 100\sqrt{\frac{[(q_{e\,\exp} - qe\ Cal)/qe\ exp]^2}{N-1}} \qquad (26)$$

Where N is the number of data points, qe exp and qe,cal (mg/g) are the experimental and calculated equilibrium adsorption capacity values, respectively.

The $\Delta q_e$ (%) obtained for PFO model ranged between 22.80 - 49.71 %, which is relatively high as compared to the $\Delta q_e$ (%) values of 4.58 – 7.27 % obtained for PSO kinetic model. In a similar way, the $\Delta q_e$ (%) obtained for Elovic model was 52.87 – 60.92 %. Based on the highest $R^2$ values that approached unity with lowest $\Delta q_e$ (%) value, the PSO model was most suitable for describing the adsorption kinetics. similar study is reported (Jeyakumar, and Chandrasekaran, 2014).

**Adsorption Isotherms**

**Langmuir Model**

Fig. 9 (a & b) display the results of Langmuir model used to determine the values of $q_m$, b and $R^2$ from the linear regression plot. The separation factor or equilibrium parameter, $R_L$, defined by Weber and Chakkravorti (Hameed *et al*., 2008) expressed in equation (19) was determined and interpreted according to the type of isotherm as $R_L > 1$, unfavorable; $R_L = 1$, linear and $0 < R_L < 1$, favorable; $R_L = 0$, Irreversible. The result of equilibrium parameter, $R_L$ for the isotherm is shown in Table 8.

$$R_L = \frac{1}{1+bC_0} \qquad (27)$$

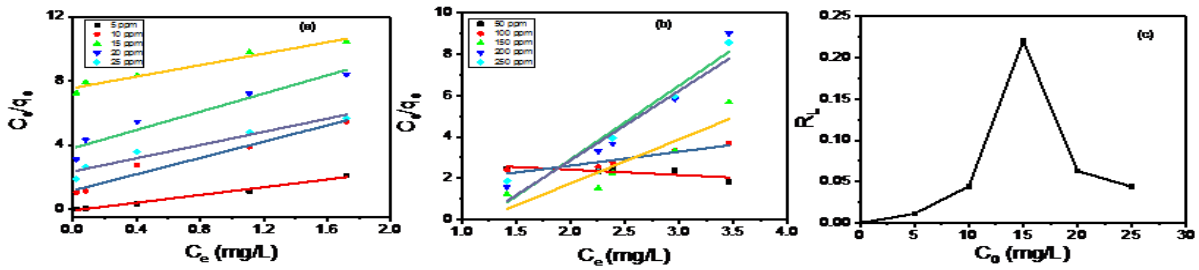


**Fig. 9: Langmuir Isotherm for the Effect of (a) MB concentration (b) Ni-$SrZrO_3$ Dosage and (c) Effect of MB Initial concentration on separation factor ($R_L$)**

Fig. 9c represents the graph of $R_L$ values verses initial MB concentration. All the $R_L$ values were between 0 and 1, indicating a favorable condition. However, as the initial concentration increased from 5 to 25 mg/L, the $R_L$ values increased from 0.0116 to 0.2204. This indicated that adsorption was favorable at higher concentrations.

**Freundlich Model**

The result of the linear plot of Freundlich model (Fig. 10) for $K_F$, n and $R^2$ values is shown in Table 8. The values for 1/n for Freundlich model are below 1, indicating a normal Langmuir isotherm. Comparing the values of correlation coefficient for Langmuir and Freundlich (Table 8), the result best described that the adsorption of MB on the catalyst is homogeneous. In addition, Freundlich constant *n*, was negative indicating that the catalyst surface is homogeneous.

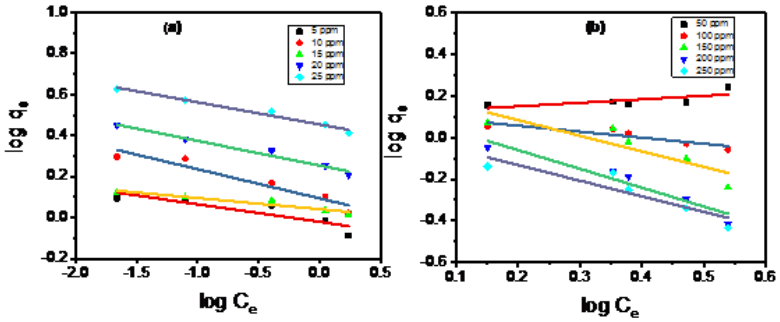


**Fig. 10: Freundlich Isotherm for Effect of MB concentration and Ni-SNZ Dosage on the adsorption of MB at 30℃**

**Table 8: Comparison of Langmuir and Freundlich Adsorption Isotherm Parameters for the Adsorption of MB dye for the effect of initial MB concentration and catalyst dosage**

| | Langmuir | | | | | Freundlich | | | |
|---|---|---|---|---|---|---|---|---|---|
| MB (mg/L) | $R^2$ | $q_m$ | b | $R_L$ | $q_e$ exp. | $R^2$ | 1/n | $k_F$ | $q_{eexp}$ |
| 5 | 0.9890 | 0.8287 | 17.4704 | 0.0113 | 1.0966 | 0.7742 | -0.0857 | 0.9537 | 1.0966 |
| 10 | 0.9714 | 0.3950 | 2.1528 | 0.0444 | 1.4491 | 0.9200 | -0.1421 | 1.2408 | 1.4491 |
| 15 | 0.9593 | 0.5614 | 0.2358 | 0.2204 | 1.3386 | 0.9172 | -0.0542 | 1.0991 | 1.3386 |
| 20 | 0.9421 | 0.3531 | 0.7434 | 0.0630 | 2.8130 | 0.9747 | -0.1202 | 1.7924 | 2.8130 |
| 25 | 0.9470 | 0.4867 | 0.8702 | 0.0439 | 4.2348 | 0.9746 | -0.1085 | 2.8439 | 4.2348 |
| mg | | | | | | | | | |
| 50 | 0.5943 | 3.8775 | 0.0880 | -2.2729 | 1.7512 | 0.4789 | -0.1676 | 1.3089 | 1.7512 |
| 100 | 0.9037 | 1.4883 | 0.5308 | 0.2737 | 1.1429 | 0.8263 | -0.2903 | 1.3041 | 1.1429 |
| 150 | 0.8343 | 0.4697 | 0.8474 | 0.3089 | 1.1820 | 0.7807 | -0.7510 | 1.7136 | 1.1820 |
| 200 | 0.9294 | 0.2806 | 0.8448 | 0.3102 | 0.8961 | 0.9226 | -0.9052 | 1.3204 | 0.8961 |
| 250 | 0.8826 | 0.2971 | 0.8696 | 0.2987 | 0.7283 | 0.8207 | -0.7525 | 1.0423 | 0.7283 |

**Dubinin Radushkevich (D-R)**

This model makes approximations for porosity, free energy, and adsorbent properties. Fig. 11 showed the result of the linear plot of D-R isotherm. The mean free energy E, of adsorption (kJ/mol) is exothermic (Table 9) for the effects of initial MB concentrations, catalyst dosage and solution pH at 30 ℃ indicating a physisorptive process (Siyasukh *et al*., 2018).

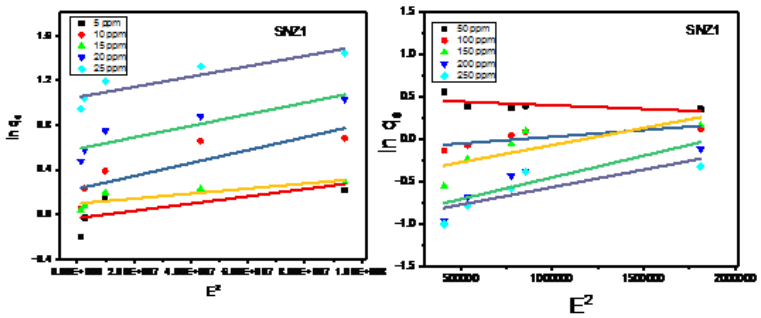


**Fig. 11: Fitted D-R Isotherm Plots for Effect of MB concentration and Ni-SNZ dosages on the adsorption of MB on Ni doped $SrZrO_3$ at 30 ℃**

**Temkin Model**

Fig.12 depicts Fitted Temkin isotherm plots for effects of initial MB concentration, catalyst dosage and solution pH. The heat of adsorption of all the molecules in the layer was negative and decrease linearly indicating an exothermic process (Table 9). The energy of reaction for D-R (kJ/mol) and Temkin (kJ/mol) for the adsorption/photocatalysis process was negative indicating an exothermic process (Table 9).

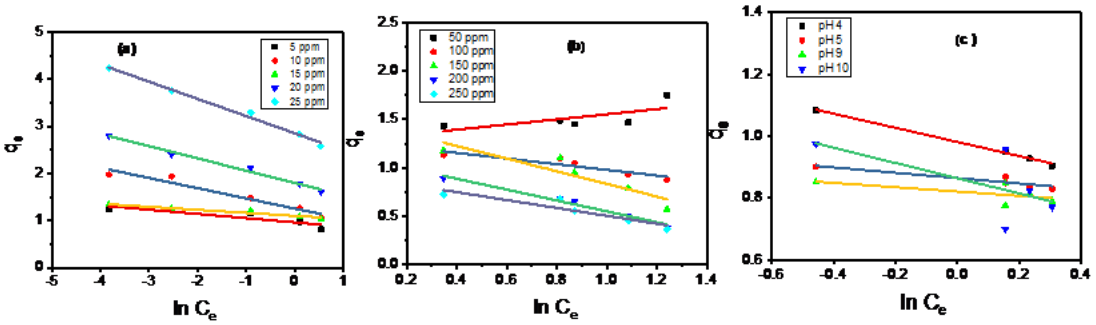


**Fig.12: Fitted Temkin Isotherm Plots for Effect of MB concentration, catalyst dosage and solution pH on Degradation of MB by Ni doped $SrZrO_3$ at 30 ℃.**

**Flory- Huggins**

Figure 13a depicts the linear fit for the model used for the calculation Flory- Huggins constants. The free energy change for the adsorption was negative, indicating a spontaneous process (Table 10).

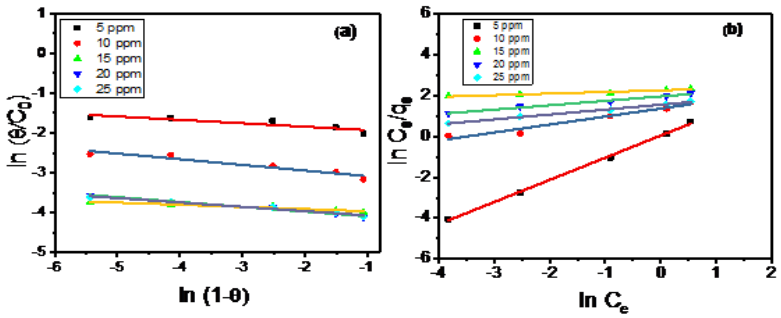


**Fig. 13: Linear Fit of (a) Flory-Huggins (b) Redlich-Peterson**

**Table 9: Comparison of D-R and Temkin Adsorption Isotherm Parameters for the effect of initial MB concentration, catalyst dosage and solution pH**

| MB (mg/L) | D-R parameters | | | | | | Temkin parameters | | | |
|---|---|---|---|---|---|---|---|---|---|---|
| | $R^2$ | $q_m$ | β | E (kJ/mol) | $q_{eExp}$ | Δ $q_e$ (%) | $R^2$ | $b_T$ ($kJmol^{-1}$) | $K_T$ ($Lmg^{-1}$) | $q_{eExp.}$ |
| 5 | 0.51966 | 0.96823 | -3.25584E-9 | -12.3923 | 1.09657 | 8.28 | 0.8082 | -28.1374 | 2.13E-05 | 1.0966 |
| 10 | 0.71003 | 1.25738 | -5.78821E-9 | -9.29422 | 1.44911 | 9.36 | 0.9445 | -11.6665 | 0.00298 | 1.4491 |
| 15 | 0.73156 | 1.103426 | -2.24203E-9 | -14.9336 | 1.3386 | 12.43 | 0.9309 | -39.3002 | 3.47E-08 | 1.3386 |
| 20 | 0.83919 | 1.797685 | -5.17154E-9 | -9.83275 | 2.81296 | 25.52 | 0.9875 | -9.67561 | 0.000997 | 2.8130 |
| 25 | 0.82452 | 2.854938 | -4.62588E-9 | -10.3965 | 4.23482 | 23.04 | 0.9900 | -6.91369 | 0.000396 | 4.2348 |
| **mg** | | | | | | | | | | |
| 50 | 0.33312 | 1.633541 | -8.5874E-8 | -2.41298 | 1.75119 | 4.75 | 0.4694 | -9.50799 | 0.007735 | 1.7512 |
| 100 | 0.65885 | 0.880522 | -1.5923E-7 | -1.77202 | 1.14292 | 16.23 | 0.8407 | -8.61599 | 0.012892 | 1.1429 |
| 150 | 0.60373 | 0.623616 | -4.0571E-7 | -1.11014 | 1.18204 | 33.41 | 0.8326 | -3.85868 | 0.102384 | 1.1820 |
| 200 | 0.78673 | 0.38212 | -5.1354E-7 | -0.98673 | 0.89608 | 40.56 | 0.9788 | -4.49197 | 0.137444 | 0.8961 |
| 250 | 0.65837 | 0.376059 | -4.1406E-7 | -1.09889 | 0.72832 | 34.20 | 0.8486 | -6.19502 | 0.106099 | 0.7283 |
| **pH** | | | | | | | | | | |
| 4 | 0.97041 | 0.844509 | -4.42344E-8 | -3.3621 | 1.0918 | 16.02 | 0.9941 | -11.0373 | 0.013582 | 1.0918 |
| 5 | 0.83316 | 0.810641 | -1.90008E-8 | -5.1298 | 0.90562 | 7.42 | 0.8789 | -29.1939 | 4.47E-05 | 0.9056 |
| 9 | 0.38282 | 0.776375 | -1.64204E-8 | -5.5182 | 0.85311 | 6.36 | 0.4015 | -36.0238 | 8E-06 | 0.8531 |
| 10 | 0.37407 | 0.712518 | -5.52665E-8 | -3.0078 | 0.98200 | 19.40 | 0.4060 | -10.2255 | 0.030015 | 0.9820 |

**Redlich-Peterson**

Fig. 13b depicts the linear fit for Redlich-Peterson used in computing its constants. Table 10 depicts the calculated values of β component of R-P and showed that it lies between the range of 1 and 0.2151 for initial MB concentration indicating the Langmuir model.

**Table 11: Flory-Huggin and Redlich-Peterson models Parameters for the Adsorption of MB dye for the effect of initial MB concentration**

| MB | | | Flory-Huggins parameters | | | Redlich- Peterson parameters | | | |
|---|---|---|---|---|---|---|---|---|---|
| (mg/L) | $R^2$ | n | $K_{FH}$ ($Lmol^{-1}$) | $\Delta G^0$ (kJ/mol | $q_{eExp.}$ | $R^2$ | β ($Lmg^{-1}$) | $K_{RP}$ | $q_{eExp.}$ |
| 5 | 0.77423 | -0.08572 | 0.133125 | -5.07977 | 1.0966 | 0.99819 | 1.0857 | 0.9537 | 1.096572 |
| 10 | 0.92005 | -0.14212 | 0.039602 | -8.13398 | 1.4491 | 0.95402 | 0.3913 | 0.2539 | 1.449112 |
| 15 | 0.91716 | -0.05415 | 0.017980 | -10.1231 | 1.3386 | 0.92376 | 0.0794 | 0.1039 | 1.338600 |
| 20 | 0.97473 | -0.10848 | 0.014793 | -10.6146 | 2.8130 | 0.98508 | 0.2151 | 0.1402 | 2.812965 |
| 25 | 0.97456 | -0.10848 | 0.015308 | -10.5284 | 4.2348 | 0.99116 | 0.2406 | 0.2100 | 4.234820 |

## CONCLUSION

In this study Nickel doped $SrZrO_3$ perovskite prepared by sol-gel Pechini method was characterized using XRD, FE-SEM, FTIR, EDX and UV-visible spectrophotometer. Photocatalytic investigation showed that the catalyst can be effectively used for the degradation of MB. The batch study parameters were pH of solution, irradiation time, initial MB concentration and catalyst dosage were found to be effective on the adsorption and degradation efficiency of MB dye. The optimized time for the degradation studies was 150 min. The degradation efficiency was greater than 80% under visible light and lower than 40% in the dark. The PFO, PSO, Elovic, intraparticle diffusion kinetic models were used for the mathematical description of the adsorption kinetics. The result showed that PSO kinetic model is predominant. The Langmuir Freundlich, D-R, Temkin, Flory-Huggins and Redlich-Peterson isotherm models were used for describing the type of isotherms. The system exhibited monolayer adsorption. The mean free energy of the reaction for D-R (kJ/mol) and Temkin (kJ/mol) for the adsorption/photocatalysis process was negative indicating an exothermic process and physisorptive. The system was said to spontaneous. The study revealed that Nickel doped strontium zirconate perovskite photocatalyst has much potential as a catalyst for the degradation of MB dye in aqueous solution.

## REFERENCES


Abebe, B., Murthy, H.C.A. and Amare, E. (2018). Summary on Adsorption and Photocatalysis for Pollutant Remediation. *Journal of Encapsulation and Adsorption Sciences* 8:225 – 255.

Alammar, T., Hamm, I., Wark, M., Mudring, A.-V. (2015). Low-temperature route to metal titanate perovskite nanoparticles for photocatalytic applications, *Appl. Catal. B* 178:20-28.

Alfonso-Herrera, L. A., Huerta-Flores, A. M., Torrez-Matinez, L. M., Rivera-Villannueva, J. M. and Ramirez-Herrera, D. J. (2018). Hybrid $SrZrO_3$-MOF Heterostructure: Surface Assembly and Photocatalytic Performance for $H_2$ Evolution and Degradation of Indigo Carmine Dye, *Journal of Materials Science: Materials in Electronics*, Springer, 29:10395–10410.

Andrades, R. C., Júnior, A. H. M., de Miranda, L. F. and Rocha, R. A. (2018). Preparation and Characterization of $Pb(Zr,Ti)O_3$ Obtained by the Pechini Method. *Materials Science Forum,* 912:97-101

Anas, M., Ali, A., Khan, A. G., Alhodaib, A., Zaman, A., Ahmad, T., Tirth, V., Algahtani, A., Ahmad, S., Abdullaeva, B. S., Al-Mughanam, T.and Aslam, M. (2023). Influence of Zirconium ($Zr^{4+}$) Substitution on the Crystal Structure and Optical and Dielectric Properties of $Sr_{0.8}Mg_{0.2}(Sn_{1-x}\ Zr_x)O_3$ Ceramics. *ACS Omeg,* 8:33794-33801

Askari, N., Jamalzdeh, M., Askari, A., Liu, N., Samali, B., Sillanpaa, M., Sheppard, L. and Li, H. (2024). Unveiling the Photocatalytic Marvels: Recent Advances in Solar Heterojunctions for Environmental Remediation and Energy Harvesting. *Journal of Environmental Sciences,* 148:283-297.

Bae, S., Kim, S., Lee, S. and Choi, W. (2014). Dye Decolorization Test for the Activity Assessment of Visible Light Photocatalysts, *Cataylsts Today*. 224:21-28.

Bellam, J. B., Ruiz-Preciado, M. A., Edely, M., Szade, J., Jouanneaux, A. and Kassiba, A.H. (2015).Visible-light photocatalytic activity of nitrogen-doped $NiTiO_3$ thin films prepared by a co-sputtering process, *RSC Adv*. 5:10551–10559.

Bello, O. S., Adelaide, O. M., Hammed, M. A. and Popoola, O. A. M. (2009). Kinetic and Equilibrium Studies of Methylene Blue Removal from Aqueous Solution by

Adsorption on Treated Sawdust. *Macedonia Journal of Chemical Engineering*, 29:77-85

Bhardwaj, N., Gaur, A., Yadav, K. (2017). Effect of Doping on Optical Properties in $BiMn_{1-2x}(TE)_xO_3$ and Sol-gel Methods. *Applied Physics A*: Volume 123, article number 429.

Boruah, P. K., Borthakur, P., Darabdhara, G., Kamaja, C.K., Karbhal, I., Shelke, M. V., Phukan, P., Saikiad, D. and Das, M. R. (2016). Sunlight Assisted Degradation of Dye Molecules and Reduction of $Cr^{6+}$ in Aqueous Medium. *RSC Advances*. *6*(13):11049-11063.

Cabello, G., Lillo, L., Caro, C., Buono-Core, G. E., Chornik, B., Flores, M., Carrasco, C. Rodriguez, C. A. (2014). Photochemical Synthesis of $AZrO_{3-X}$ thin films (A=Ba, Ca and Sr) and their Characterization. *Ceramics International* 40:7761–7768.

Chang, C.W. and Hu, C.C. (2020). Graphene oxide-derived carbon-doped $SrTiO_3$ for highly efficient photocatalytic degradation of organic pollutants under visible light irradiation, *Chem. Eng. J*. 383,123116.

Edet, U. A. and Ifelebuegu, A. O. (2020). Kinetics, Isotherms and Thermodynamic Modelling of the Adsorption of Phosphates from Model Wastewater using Recycled Brick Waste, *Processes*, 8 (665):1-15.

Eneji, I.S., Julian, N. and Sha'Ato, R. (2016). Kinetic and Thermodynamic Study of Aqueous Adsorption of $Cd^{2+}$ and $Pb^{2+}$ ions on Activated Carbon from *Nymphaea ampla* (Water Lily) Roots, *FUW Trends in Science & Technology Journal*, 1 (2):456 – 465.

Hameed, B. H., Tan, I.A. W. and Ahmad, A. L. (2008). Adsorption Isotherm, Kinetic modeling and Mechanism of 2, 4, 6, Trichlorophenol on Coconut husk-based Activated Carbon. *Chemical Engineering Journal* 144:235-244.

Habisreutinger, S. N., Schmidt-Mende, L. and Stolarczyk, J. K. (2013). Photocatalytic Reduction of $CO_2$ on $TiO_2$ and other Semiconductors. *Angew. Chem., Int. Ed*. 52 (29):7372-7408.

Hu, Y., Mao, L., Guan, X., Tucker, K. A., Xie, H., Wu, X. and Shi, J. (2020). Layered Perovskite Oxides and Their Derivative Nanosheets Adopting Different Modification Strategies Towards Better Photocatalytic Performance of Water Splitting, *Renewable Sustainable Energy Rev*., 119, 109527.

Huang, J., Zhou, L., Wang, Z., Lan, Y., Tong, Z., Gong, F., Sun, J. and Li, L. (2009). Photoluminescence Properties of SrZrO3:$Eu^{3+}$ and $BaZrO_3$:$Eu^{3+}$ Phosphors with Perovskite Structure. *Journal of Alloys Compound*, 487:5-7

Itodo A.U., Aondofa B. G. and Iorungwa M. S. (2018). Retarding Mild Steel Corrosion using a Blend of Schiff Base Metal Complex and Neem Plant Extract. *ChemSearch Journal*, 9(2): 45 – 63.

Jain, K., Patel, A. S., Pardhi, V. P. and Flora, S. J. S. (2021). Nanotechnology in Wastewater Management: a New Paradigm Towards Wastewater Treatment. *Molecules* 26, 1797.

Jiang, J., Jia, Y., Wang, Y., Ruifeng Chong, R., Xu, L. and Liu, X. (2019). Insight into efficient photocatalytic elimination of tetracycline over $SrTiO_3$(La,Cr) under visible-light irradiation: The relationship of doping and performance, *Applied Surface Science*,486-93-101.

Jiang, D., Xu, P., Wang, H., Zeng, G., Huang, D., Chen, M., Lai, C., Zhang, C., Wan, J. and Xue, W. (2018). Strategies to Improve MOFs photocatalyst's Performance for Degradation of Organic Pollutants, *Coordination. Chem. Rev*., 376:449 466.

Jeyakumar, R. P. S. and Chandrasekaran, V. (2014). Adsorption of $Pb^{2+}$ by Activated Carbons Prepared from Marine Gree Algae: Equilibrium and Kinetic Studies. *International Journal Industrial Chemistry*, 5,10.

Jubu, P. R., Yam, F. K. and Low, K.T. (2020). Feasibility Study on Synthesis of $G_2O_3$ Nanostructures on Glass Substrate by Chemical Vapor Deposition, *Thin Solid Films* 10:1–7.

Jubu, P.R., Yam, F.K. and Chahrour, K.M. (2020). Structural and morphological properties of β-$Ga_2O_3$ nanostructures synthesized at various deposition temperatures, *Physica E: Low-Dimensional Systems and Nanostructures* 123: 1–8.

Kajjumba, G. W., Emik, S., Öngen, A., Özcan, H. K.. and Aydın, S. (2018). Modelling of Adsorption Kinetic Processes—Errors, Theory and Application. *Advanced sorption process applications*, 1-19.

Katyayan, S. and Agrawal, S. (2017). Investigation of Spectral Properties of $Eu^{3+}$ and $Tb^{3+}$ doped $SrZrO_3$ Orthorhombic Perovskite for Optical and Sensing Applications. *Journal of Materials Science: Materials in Electronics*, *28*(24):18442-18454.

Kong, X. Y., Lee, W. Q., Mohamed, A. R. and Chai, S. P. (2019). Effective Steering of Charge Flow through Synergistic Inducing Oxygen Vacancy Defects and pn Heterojunctions in 2D/2D Surface-Engineered $Bi_2WO_6$/BiOI Cascade: Towards Superior Photocatalytic $CO_2$ Reduction Activity. *Chemical Engineering Journal*, 372:1183-1193.

Kumar, S., Kumar, A., Bahuguna, A., Sharma, V. and Krishnan, V. (2017). Two-Dimensional Carbon-Based Nanocomposites for Photocatalytic Energy Generation and Environmental Remediation Applications, *Beilstein Journal of Nanotechnology*, (8 (1):1571-1600.

Lucena, G. L., de Lima, L. C., Honorio, M. C., de Oliveira, A. L. M., Transqiilim, R. L., Longo, E., de Souza, A. G., da Maia, A. S. and dos Santos, I. M. G. (2017). $CaSnO_3$ obtained by Modified Pechini Method Applied in te Photocatalytic Degradation of an Azo Dye. *Ceramica* 63:536-54.

Luo, J., Li, R., Chen, Y., Zhou, X., Ning, X., Zhan, L., Ma, L., Xu, X., Xu, L. and. Zhang, L. (2019). Rational Design of Z-scheme $LaFeO_3/SnS_2$ Hybrid with boosted Visible Light Photocatalytic Activity towards Tetracycline Degradation. *Separation and Purification Technology*, 210:417–430.

Mantwa A. L., Kamohelo G. T., Selepe J. M., Iorkyaa A. and Odireleng M. N. (2018). Study on Photoluminescence and Energy transfer of $Eu^{3+}/Sm^{3+}$ single-doped and co-doped $BaB_8O_{13}$ Phosphors, *Physica B: Physics of Condensed Materials.* 535:89-95.

Musah, M., Azeh, Y., John T. Mathew, J. T., Musa T., Umar, M. T., Abdulhamid, Z. and Muhammad, A. I. (2022). Adsorption Kinetics and Isotherm Models. *CaJoST*, 1:20-26.

Nakada, N., Hanamoto, S., Jürgens, M.D., Johnson, A.C., Bowes, M. J. and Tanaka, H. (2017). Assessing the population equivalent and performance of wastewater treatment through the ratios of pharmaceuticals and personal care products present in a river basin: application to the River Thames basin, UK, *Sci. Total Environ*. 575:1100–1108.

Nechifor, G., Pascu, D., Neagu, M.P., Traistaru, G.A. and Albu, P.C. (2015). Comparative Study of Temkin and Flory-Huggins Isotherms for Adsorption of Phosphate Anion on Membranes. *UPB Scientific Bulletin*, 77:63-72.

Nguyen, T. T. T., Nguyen, T. N., Tran, Q. V., Nguyen, H. K., Nguyen, M. T. and Le, T. H. N. (2016). Synthesis, Characterization and Effect of pH on degradation of dyes of Cu-doped $TiO_2$, *J. Exp. Nanosci.*, 11:226–238223

Obaid, S. A. (2020). Langmuir, Freundlich and Tamkin Adsorption Isotherms and Kinetics for the Removal of *aartichoke tournefortii* straw from Agricultural Waste. *Journal of Physics*: Conference Series, 1664 012011.

Ouni, S., Nouri, S., Rohlicek, J. and Hassen, R. B. (2012). Structural and Electrical Properties of the Sol-gel Prepared $Sr_{1-x}Er_xSnO_{3-\delta}$ Compounds. *J. Solid State Chem*,192:132-138.

Patil, S. D., Renukdas, S. and Patel, N. (2012). Comparative Study of Kinetics of Adsorption of Methylene Blue from Aqueous Solutions using Cinnamon plant (*Cinnamonum zeylanicum*) Leaf Powder and Pineapple (*Ananas comosus*) peel powder, *The Electronic Journal of Chemistry*, 4(2):77-100.

Perumal, V., Sabarinathan, A., Robert, R., Prabu, K. M. and Uthirakumar, R. (2012). Facile synthesis of cationic surfactant-treated hierarchical nanorods $SnO_2$@CdO nanocomposite photocatalyst for degradation of methylene blue under sunlight. *Materials Today* 234:223- 331.

Rani B., Thamizharasan, G., Nayak, A. K and Sahu, N. K. (2020). In: Photocatalysts in Advanced Oxidation Processes for Wastewater Treatment. Edited by Elvis Fosso-Kankeu, Sadanand, P and Supraskas, S.H. Scriener Publishing Wiley. Pp.197-257.

Rashad, M., Helali, S., Issa, S., Al-Ghamdi, S., Alsharif, M., Alzahrani, A. O. and Abd-Elnaiem, A. M. (2022). Adsorption Study of Congo Red Dye from Synthetic Wastewater at Different Concentrations Using Zinc Sulfide Nanoparticles. *Materials*, *15*(14), 5048.

Rojas-Cervantes, M. L. and Castillejos, E. (2019). Perovskites as Catalysts in advanced Oxidation Processes for Wastewater Treatment, *Catalysis* 9:230–268.

Safari, S., Ahmadian, S. M. S. and Amani-Ghadim, A. R. (2020). Visible Light Photocatalytic Activity Enhancing of $MTiO_3$ Perovskites by M-cation (M = Co, Cu and Ni) Substitution and Gadolinium Doping, *Journal of Photochemistry and Photobiology* A: *Chemistry*, 394, 112461.

Saha, D., Desipio, M. M., Hoinkis, T. J., Smeltz, E. J., Thorpe, R., Hensley, D. K., Fischer-Drowos, S. G. and Chen, J. (2018). Influence of $H_2O_2$ in Enhancing Photocatalytic Activity of Carbon Nitride under Visible Light: *Journal of Environmental Chemical Engineering*, https://doi.org/10.1016/j.jece.2018.07.030

Singh, M., Kumar, A. and Krishnan, V. (2020). Influence of Different Bismuth Oxyhalides on the Photocatalytic Activity of g-$C_3N_4$. *Materials Advances*, **1**:1262-1272.

Singh, J., Verma, V., Kumar, R. and Kumar, R. (2019). Influence of $Mg^{2+}$ Substitution on the Optical Band Gap Energy of $Cr_{2-x}Mg_{2-}$

$_xO_3$ Nanoparticles. *Results in Physics*, 13, 102106.

Siyasukh, A., Chimupala, Y. and Tonanon, N. (2018) Preparation of Magnetic Hierarchical Porous Carbon Spheres with Graphitic Features for High Methyl Orange Adsorption Capacity. *Carbon*, 134:207-221.

Soltanabadi, Y., Jourshabani, M. and Shariatinia, Z. (2018). Synthesis of novel CuO/$LaFeO_3$ nanocomposite photocatalysts with superior Fenton-like and visible-light photocatalytic activities for degradation of aqueous organic contaminants, *Sep. Purif. Technol*. 202:227–241.

Subramanian, Y., Mishra, B., Mandal, S., Gubendiran, R. and Chaudhary, Y. S. (2020). Design of heterostructured perovskites for enhanced photocatalytic activity: Insight into their charge carrier dynamics. *Materials Today: Proceedings*

Tarrida, M., Larguem, H. and Madon, M. (2009). Structural Investigations of (Ca,Sr)$ZrO_3$ and Ca(Sn,Zr)$O_3$ Perovskite Compounds. *Physics and Chemistry of Minerals* 36:403-413.

Triyona, D., Hanifaha, U. and Laysandra, H. (2020). Structural and optical properties of Mg-substituted $LaFeO_3$ nanoparticles prepared by a sol-gel method. *Results in Physics* 16, 102995.

Trocha, A., Impert, O., Katafias, A. and Van-Eldik, R. (2021). Mechanistic details of the catalytic degradation of MB by $H_2O_2$ in basic solution. *Polyhedron* 210, 115507.

Utami, R. W., Rafsanjani, R. A. and Triyono, D. (2019). Optical Properties of $La_{0.9}Sr_{0.1}Fe_{1-x}Mo_xO_3$ (x = 0.1, 0.2, and 0.3) Perovskite Material Prepared by Sol-gel Method. *J. Phys*. 1153, 012072.

Vettumperumal, R., Kalyanaraman, S., Santoshkumar, B. and Thangavel, R., (2016). Estimation of Electron–phonon coupling and Urbach energy in Group 1 Elements doped ZnO Nanoparticles and Thin Films by Sol-gel Method. *Materials Research Bulletin*, 77:101-110.

Yazdanbakhsh, M., Tavakkoli, H. and Hosseini, S. M. (2011). Characterization and Evaluation Catalytic Efficiency of $La_{0.5}Ca_{0.5}NiO_3$nanopowders in Removal of Reactive blue 5 from Aqueous Solution, *Desalination* 281:88–395.

Wang, S., Yang, X., Zhang, X., Ding, X., Yang, Z., Dai, K. and Chen, H. (2017). A plate-on-plate sandwiched Z-scheme heterojunction photocatalyst: BiOBr-$Bi_2MoO_6$ with enhanced photocatalytic performance. *Appl. Surf. Sci*. 391:194-201.

Wei, K., Faraj, Y., Yao., Xie, R. and Lai, B. (2021). Strategies for Improving Perovskite Photocatalysts Reactivity for Organic Pollutants Degradation. *Chemical Engineering Journal*, *414*, 128783.

Wu, Z., Yu, C., Liu, R., Dionysiou, D. D., Yang, K., Wang, C. and Liu, H. (2017). Novel Fluorinated $Bi_2MoO_6$ Nanocrystals for Efficient Photocatalytic Removal of Water Organic Pollutants under Different Light Source Illumination. *Applied Catalysis B: Environmental*, 209:1-11.

Zhang,W., Yang, S., Li, J., Gao, W., Deng, Y., Dong, W., Zhao, C., Lu, G. (2017) Visible-to ultraviolet Up-conversion: energy transfer, material matrix, and synthesis Strategies, *Appl. Catal. B Environ*. 206:89–103

Zeng, S., Kar, P., Thakur, U. K. and Shankar, K. (2018). A Review on Photocatalytic $CO_2$ Reduction using Perovskite Oxide Nanomaterials. *Nanotechnology* 29 (5), 052001.